Global Precipitation at One-Degree Daily Resolution from Multisatellite Observations

GEORGE J. HUFFMAN,*+ ROBERT F. ADLER,* MARK M. MORRISSEY,# DAVID T. BOLVIN,*+
SCOTT CURTIS,*@ ROBERT JOYCE,&** BRAD MCGAVOCK,# AND JOEL SUSSKIND*

* *Laboratory for Atmospheres, NASA Goddard Space Flight Center, Greenbelt, Maryland*
+ *Science Systems and Applications, Inc., Lanham, Maryland*
# *Environmental Verification and Analysis Center, Norman, Oklahoma*
@ *Joint Center for Earth Systems Technology, University of Maryland, Baltimore County, Baltimore, Maryland*
& *Climate Prediction Center, NOAA/NWS/NCEP, Washington, D.C.*
** *Research and Data Systems Corp., Greenbelt, Maryland*

(Manuscript received 11 April 2000, in final form 9 October 2000)

ABSTRACT

The One-Degree Daily (1DD) technique is described for producing globally complete daily estimates of precipitation on a 1° × 1° lat/long grid from currently available observational data. Where possible (40°N–40°S), the Threshold-Matched Precipitation Index (TMPI) provides precipitation estimates in which the 3-hourly infrared brightness temperatures (IR T_b) are compared with a threshold and all ''cold'' pixels are given a single precipitation rate. This approach is an adaptation of the Geostationary Operational Environmental Satellite Precipitation Index, but for the TMPI the IR T_b threshold and conditional rain rate are set locally by month from Special Sensor Microwave Imager–based precipitation frequency and the Global Precipitation Climatology Project (GPCP) satellite–gauge (SG) combined monthly precipitation estimate, respectively. At higher latitudes the 1DD features a rescaled daily Television and Infrared Observation Satellite Operational Vertical Sounder (TOVS) precipitation. The frequency of rain days in the TOVS is scaled down to match that in the TMPI at the data boundaries, and the resulting nonzero TOVS values are scaled locally to sum to the SG (which is a globally complete monthly product).

The GPCP has approved the 1DD as an official product, and data have been produced for 1997 through 1999, with production continuing a few months behind real time (to allow access to monthly input data). The time series of the daily 1DD global images shows good continuity in time and across the data boundaries. Various examples are shown to illustrate uses. Validation for individual gridbox values shows a very high mean absolute error, but it improves quickly when users perform time/space averaging according to their own requirements.

1. Introduction

A long time series of finescale observation-based global precipitation is needed to support a variety of studies, including global change, surface hydrology, and numerical weather and climate model initialization and validation. However, data record, sampling, and algorithmic considerations limit the range of scales that could be reported with reasonable accuracy. For example, the World Climate Research Programme (WCRP) established the Global Precipitation Climatology Project (GPCP) with the initial goal of producing precipitation estimates on a monthly 2.5° × 2.5° lat/long grid for a number of years (WCRP 1986). The GPCP is succeeding in this goal, with over two decades of data available (1979–99 at present), and routine production continuing a few months after real time.

Because of the lack of finer-scale precipitation data, numerous applications remain stymied. Researchers wish to validate hydrologic streamflow models by forcing them with observed data that resolve individual storms and catch basins. Even monthly scale events are hard to study with calendar-month averages. Extratropical blocking events are a typical example. They initiate and decay within the span of a few days, but can persist for weeks (Blackmon et al. 1984). Calendar-month averages typically mix blocking and nonblocking periods, whereas daily data allow the researcher to composite the data much more cleanly.

The fundamental barrier to finer-scale estimates is the lack of accurate, dense global data, either from in situ or remote sensors. Some regions do have the possibility of detailed precipitation estimates thanks to local networks of sensors, such as the Weather Surveillance Ra-

Corresponding author address: Dr. George J. Huffman, NASA Goddard Space Flight Center Code 912, Greenbelt, MD 20771.
E-mail: huffman@agnes.gsfc.nasa.gov

dar 1988 Doppler (WSR-88D) system in the United States (Crum et al. 1998). A few more regions are covered by relatively dense networks of rain gauges, but the coverage is still far short of global, even with respect to land areas. An additional barrier to daily gauge analyses is that there is no uniform standard for the time of report, even within regions. As a result, at most locations around the world it is necessary to depend on satellite-based passive sensors. Microwave radiometers on polar-orbit satellites produce fairly accurate instantaneous estimates, but their sparse temporal sampling constrains the time/space gridding needed to achieve reasonable random errors in the GPCP dataset.

Infrared (IR) radiometers on geosynchronous satellites (geo-IR) provide excellent time and space sampling, but the quantity being sensed (mostly cloud-top temperature) is indirectly connected to precipitation, particularly on the shortest time and space scales, and most acutely in extratropical latitudes. A problem that geo-IR data share with most satellite datasets is that the viewing geometry becomes unfavorable near the limb of each satellite's view. This problem can be solved in part at tropical and subtropical latitudes by merging all available geo-IR data, but the issue remains, most acutely at higher latitudes and in cases where the closest geosynchronous satellite is not reporting data. An additional barrier is the need to work with several international partners to obtain administrative permissions, maintain routine data deliveries, and dedicate sufficient computing resources before the use of global, full-resolution geo-IR data can be a reality.

Starting in October 1996, the GPCP set the stage for higher resolution estimates by working with the geosynchronous-satellite operators around the world to collect histograms of geo-IR brightness temperature (T_b) on a 1° × 1° grid covering 40°N–40°S at 3-hourly intervals. The availability of this dataset prompted the authors to develop the Threshold-Matched Precipitation Index (TMPI) to estimate precipitation from the 3-hourly geo-IR histograms, described in section 2. To complete the global coverage, a technique for estimating precipitation outside of the geo-IR coverage using sounding data from low-earth polar-orbit satellites was developed, as described in section 3. Together, these form the One-Degree Daily (1DD) dataset, which is a first approach to estimating global daily precipitation at the 1° × 1° scale from observationally based data. The philosophy is to use statistical parameters from trusted estimates to constrain the overall behavior of the 1DD estimates, and then to use the geo-IR and sounder data to determine the day-to-day behavior. In the same vein, the adjustments are computed and applied a month at a time to ensure simplicity and stability. All of the computations in this paper are carried out separately for each grid box (perhaps with some smoothing) unless otherwise stated. Section 4 provides validation results, and section 5 summarizes some examples of 1DD-based analysis.

The reader should keep in mind that the geo-IR and sounder data are responding to *clouds*, rather than *hydrometeors*, so there is a substantial algorithmic uncertainty at the finest scales. Our goal is to provide users with unprecedented flexibility in computing time or space averages according to their own requirements.

2. Threshold-Matched Precipitation Index

The Geostationary Operational Environmental Satellite (GOES) Precipitation Index (GPI; Arkin and Meisner 1987) is one popular IR technique that estimates area-averaged rainfall. It assigns the constant conditional rainrate $R_c = 3$ mm h^{-1} to all pixels within a given region that have $T_b < 235$ K, and assigns zero rain rate to all others. These constants were chosen to maximize correlations with hourly (or longer) radar-estimated rainfall on a 2.5° × 2.5° lat/long grid over the Global Atmospheric Research Program (GARP) Atlantic Tropical Experiment (GATE) ship array in summer 1974. Adler et al. (1993) held the threshold [T_b(rain)] constant and allowed R_c to vary according to calibration between (approximately) time/space-matched GPI and Special Sensor Microwave Imager (SSM/I)–based rain estimates accumulated for a month, creating the Adjusted GPI. In this paper we introduce the TMPI, which allows both T_b(rain) and R_c to vary, following the probability matching concepts in Kummerow and Giglio (1995) and Xue et al. (1999). For simplicity and stability, the (spatially varying) T_b(rain) and R_c are computed on a monthly basis in the TMPI.

The (observational) datasets used for the TMPI (Fig. 1) at present are as follows.

1) GPCP histograms of geo-IR T_b are compiled on a 1° × 1° lat/long grid over 40°N–40°S at 3-h intervals. The histograms have 24 unevenly spaced classes covering 190–270 K.
2) GPCP Advanced Very High Resolution Radiometer (AVHRR) low-earth-orbit IR (leo-IR) GPI estimates are compiled on a 1° × 1° lat/long grid over 40°N–40°S in 3-h averages.
3) The SSM/I occurrence of precipitation according to the Version 6.0 Goddard Profiling algorithm [GPROF 6.0, based on Kummerow et al. (1996)] is computed by the Goddard Space Flight Center Laboratory for Atmospheres on a 0.5° × 0.5° lat/long global grid for each orbit. GPROF is a physically based retrieval that matches observed radiances from all seven SSM/I channels to cloud-model-based radiances, producing pixel-by-pixel precipitation estimates.
4) The GPCP version 2 satellite–gauge [SG; based on Huffman et al. (1997)] combination precipitation estimates (r_{SG}) are produced on a 2.5° × 2.5° lat/long global grid by month and are box interpolated to 1° × 1° for this study. The SG applies a sequential

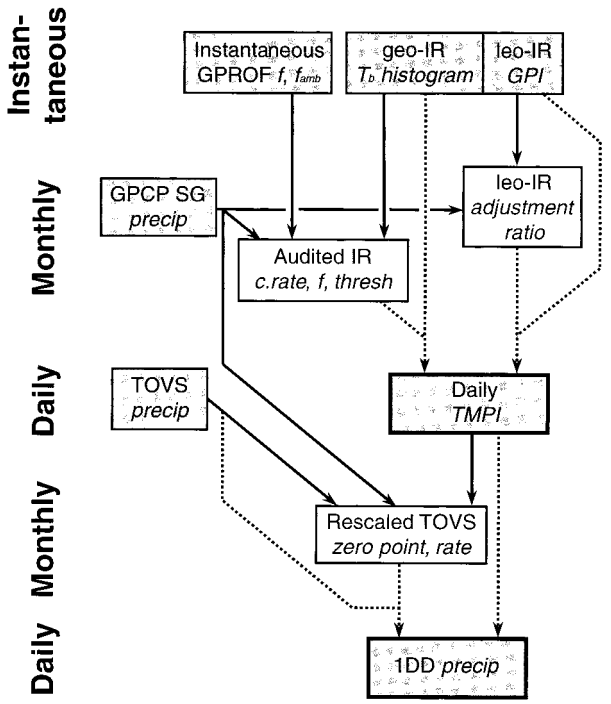

FIG. 1. Block diagram of the 1DD algorithm. The data flow for computing coefficients is shown with solid lines, and production data flow is shown with dashed lines. Gridded data fields are shaded, and the output fields are shown as boxes with heavy borders.

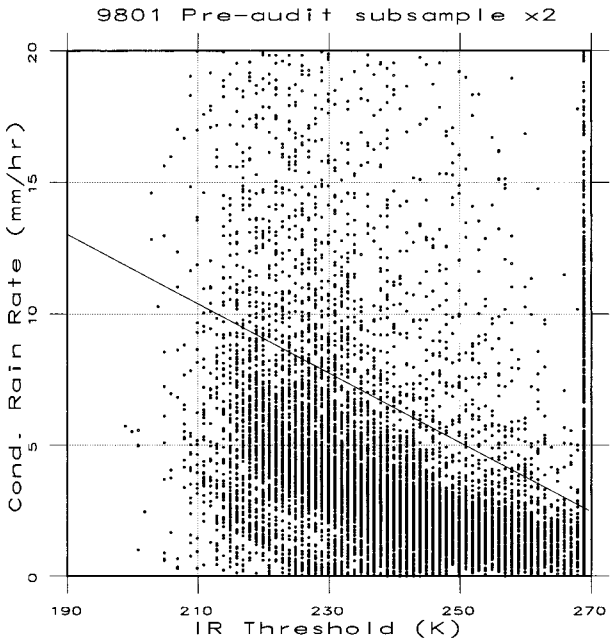

FIG. 2. Scattergram of the TMPI R_c vs T_b(rain) for Jan 1998 before any auditing is performed. The solid line defines the boundary between outliers and acceptable values (above and below the line, respectively).

combination technique to SSM/I, geo-IR, TOVS (introduced below), and rain gauge analyses.

The geo-IR histograms are interpolated to a 1-K interval (Joyce and Arkin 1997) and corrected for zenith angle effects (Joyce et al. 2001), providing an estimate of the true nadir-view IR T_bs. Both steps tend to broaden the geo-IR histograms because both involve estimating sub-bin histogram structure. Such broadening occurs equally in the calibration and estimation steps, so it likely introduces additional random error, but not bias. The revised geo-IR histograms are matched within ± 1.5 h to the microwave-based frequency of precipitation and each is accumulated for the month. To further ensure stability, the monthly matched accumulations are smoothed with a 7×7 grid-box boxcar filter. In each grid box, the geo-IR histogram is summed starting with the coldest bin until the cumulative fraction of total pixels matches the microwave-based fractional coverage, and T_b(rain) is set to the corresponding T_b. This T_b(rain) is applied to the 7×7-box-smoothed sum of *all* T_b histograms in the box for the month, yielding the fractional occurrence of rain in the full geo-IR dataset for the month, f_{IR}. The single local conditional rain rate for all raining pixels during that month is computed as

$$R_c = \frac{r_{\mathrm{SG}}}{f_{\mathrm{IR}}}, \tag{1}$$

because we require the TMPI to sum to the (monthly) SG product over the month to maintain consistency between daily and monthly products. We carry out all computations in millimeters per day, although R_c is discussed in millimeters per hour to conform to the usual representation of pixel-level precipitation.

Preliminary work showed that the T_b(rain) and R_c computed in this first round of estimation contain some unrealistic values. Various combinations of parameters were tested for diagnosing this problem, of which the plot of R_c as a function of T_b(rain) seemed the most useful. Note that most points are tightly clustered (Fig. 2), but there is a scatter of high-R_c outliers. Outliers usually occur in coherent patches (outlined with a red line in Fig. 3 for the sample month of January 1998) that tend to be associated with light precipitation totals or strong gradients in precipitation amount, likely due to sampling problems in the SSM/I data. Such values would tend to cause estimation of a few unrealistically heavy precipitation events during the month. Accordingly, an audit procedure was developed that determines new T_b(rain) that are consistent with the SG values, when required. We lack a definitive theoretical basis for identifying outliers, so we have subjectively chosen a linear cutoff that parallels the main cluster and excludes the highest 10% of boxes for the example month (Fig. 2). At this level of approximation we have neglected the hints at nonlinear behavior for low T_b(rain). The outlier R_c values are deleted and the missing values are smoothly filled from the surrounding values. The ''audited'' R_c values are used to generate audited f and then

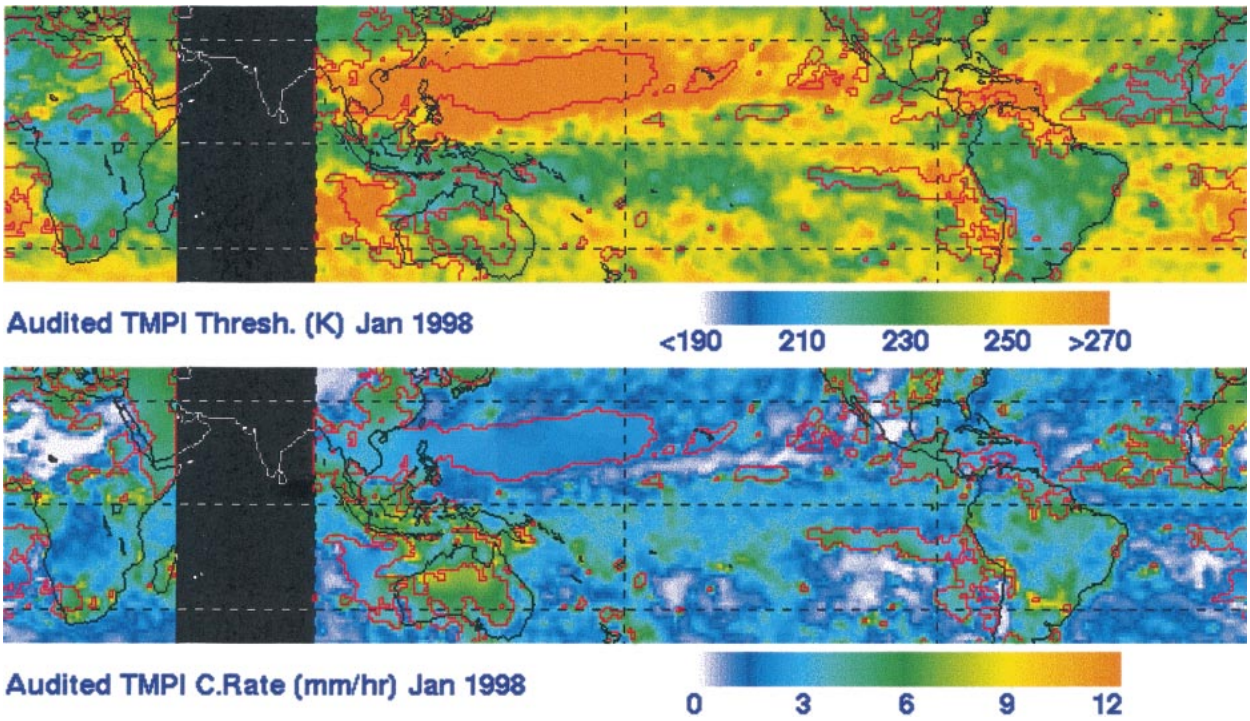

FIG. 3. Audited T_b(rain) in kelvin (top), and audited R_c in millimeters per hour (bottom) for the Jan 1998 TMPI. Blacked-out areas have no data because of a lack of geo-IR data. Red lines enclose areas that have been audited.

T_b(rain) estimates. As shown in Fig. 3, the resulting audited fields are physically reasonable. Small errors in setting these parameters are likely not crucial, since the smoothing due to $1° \times 1°$ gridding and daily summation will mask the detailed pixel-level occurrence of rain. The auditing procedure always reduces R_c and increases T_b(rain) and f [except for T_b(rain) = 269 K].

Even this auditing cannot solve all problems when T_b(rain) = 269 K, because the warmest T_b bin in the merged geo-IR dataset contains all values $\geq$ 270 K. A region with low cloud tops, such as within a subtropical high, likely should have T_b(rain) $\geq$ 270 K, but T_b(rain) must be limited to the last distinguishable temperature bin of 269 K (the uniform orange areas in Fig. 3), and will be given an artificially high R_c in the first round of estimation. Presently the auditing procedure replaces R_c outliers by (lower) smooth-filled values, even though T_b(rain) is constrained to 269 K. This prevents unreasonable instantaneous values at the cost of failing to sum to the monthly SG value. The penalty for this choice is small because nearly all cases are in low-precipitation regions. Note that the corresponding lower limit of the histogram bins (190 K) is not a problem in practice. This discussion highlights a fundamental limitation of any simple IR threshold technique—all pixels colder than T_b(rain) are labeled ''precipitating,'' and all those warmer are not. Thus, all precipitation, including that from ''shallow'' clouds, is represented in the IR approximation by the ''deep'' clouds, regardless of whether each deep cloud is actually precipitating. The warm limit becomes a problem when there are so few geo-IR pixels colder than 270 K that the precipitation areas sensed by the SSM/I cannot be replicated in the TMPI.

The final audited R_c and T_b(rain) fields (Fig. 3) provide important insights into the systematic regional variations in geo-IR data for the month. Here, R_c and T_b(rain) are near the GPI values in tropical oceanic zones with ''heavy'' precipitation, but the corresponding land areas show much colder T_b(rain) with higher R_c. This implies that heavy convection in tropical land areas is deeper and more concentrated than over tropical oceans. In the relatively dry subtropical highs T_b(rain) is warm because there is little or no penetrative convection. The relatively low T_b(rain) and R_c over the Sahara Desert help screen out nonprecipitating cirrus that passes over this region during the boreal winter. The gradients along the northern coast of Africa reflect the transition from desert to the pattern of boreal wintertime storms that typifies the Mediterranean.

Holes occur in individual geo-IR images, most routinely in the Indian Ocean sector, where no geo-IR data were available until June 1998. To compensate, leo-IR estimates from the National Oceanic and Atmospheric Administration (NOAA)–series polar-orbiting satellites are processed to fill in holes as necessary. The leo-IR data appear as GPI estimates in the GPCP merged IR dataset and depict rain areas that systematically cover too much area. We address this problem by forcing the month's fraction of rainy 3-hourly leo-IR grid-box values to match the same fraction for smoothly filled geo-

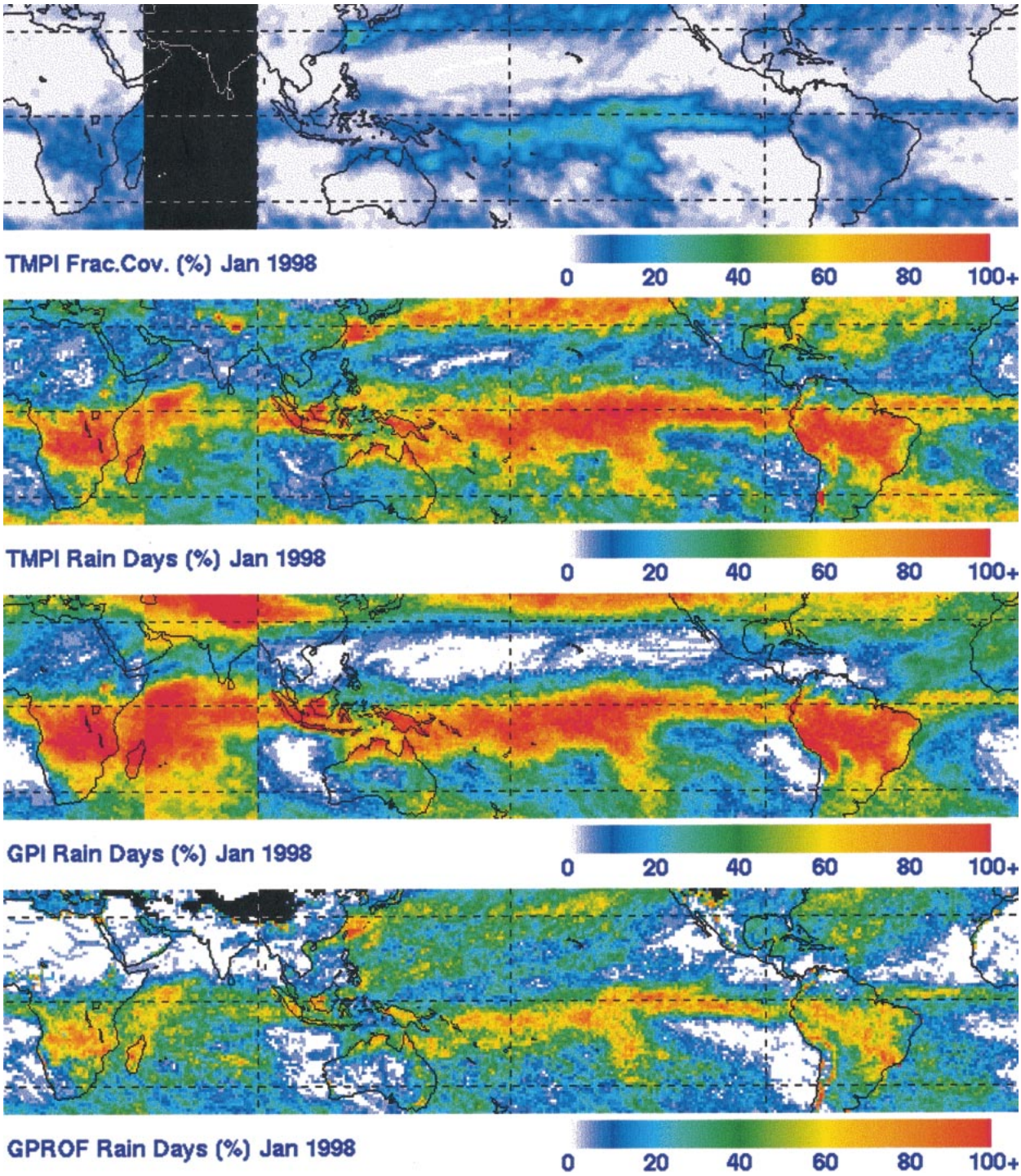

FIG. 4. Occurrence of rain as represented by the TMPI f_{rain} (top), TMPI rain days (upper middle), GPI rain days (lower middle), and GPROF rain days (bottom) in percent for Jan 1998.

IR. Similar to our TOVS adjustment (section 3), we set to zero the smallest leo-IR rain rates, then linearly rescale the remaining rates to sum to the monthly SG.

The basic output of the TMPI is a sequence of 3-hourly instantaneous estimates, mostly resulting from geo-IR. In the current release, the 3-hourly images in each day (0000 UTC, . . . , 2100 UTC) are summed to produce the daily value. The daily product is considered more reliable than individual 3-hourly images for two reasons. First, GPI-type IR estimates show better cor-

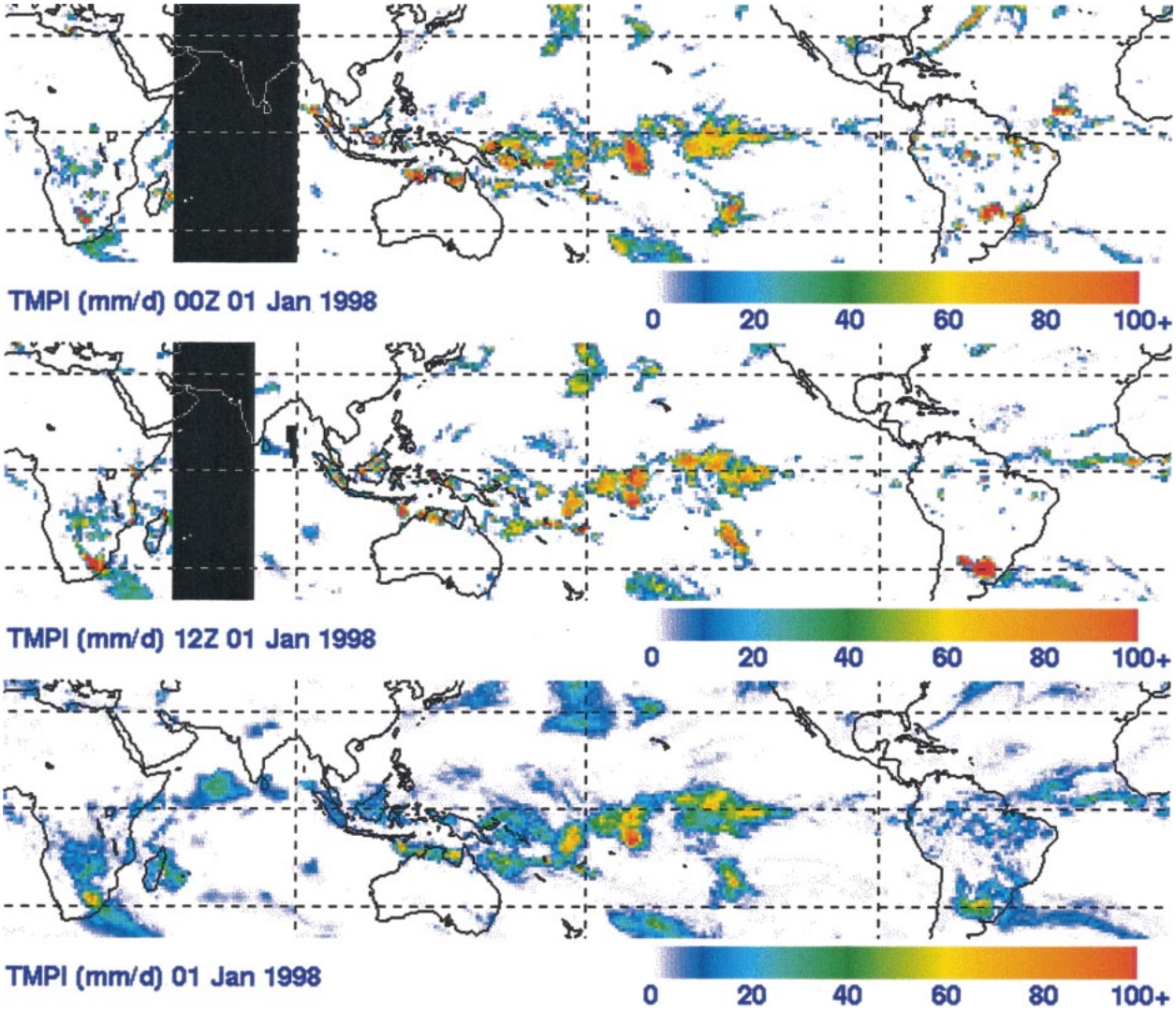

FIG. 5. Instantaneous 0000 UTC (top) and 1200 UTC (middle) TMPI, and daily TMPI (bottom) in millimeters per day for 1 Jan 1998. Blacked-out areas have no data.

relation with precipitation as the averaging period increases (Arkin and Meisner 1987). Second, the current procedure does not take into account the time of day (i.e., diurnal cycle biases). As a result, the individual 3-hourly estimates are not part of the current release.

One interesting result of the TMPI procedure is insight into the frequency of occurrence of precipitation. If we define ''fractional coverage'' as the fraction of all satellite pixels contributing to the grid box that have nonzero rain, and ''rain days'' as the fraction of days on which a grid box has nonzero rain (i.e., at least one pixel with nonzero rain sometime during the day), then we expect the fractional coverage to be less than rain days. In the case of the TMPI, the ratio of fractional coverage to rain days is less than 0.4 almost everywhere (Fig. 4). Furthermore, TMPI and GPI rain day maps are closer to each other than to the rain days apparently implied by summing GPROF over a day. Thus, ''low'' (instantaneous pixel level) fractional coverage *is* consistent with ''high'' (day-average grid-box level) rain days. This demonstrates that the generally low GPROF rain days values are the result of poor time sampling, usually one or two samples in a day, rather than indicating that the GPROF fractional coverage is unrealistically low. The results of comparing Figs. 3 and 4 also verify that TMPI rain days are higher (lower) than GPI rain days for the TMPI threshold above (below) the GPI T_b(rain) of 235 K.

We find that the instantaneous TMPI fields show good temporal and spatial consistency among images, and with the daily TMPI field (Fig. 5). As we expect, the daily fields are smoother, broader, and have lower maxima than the instantaneous fields. Tests show that the daily TMPI correctly sum to the monthly SG, except in the subtropical North Pacific, where threshold saturation

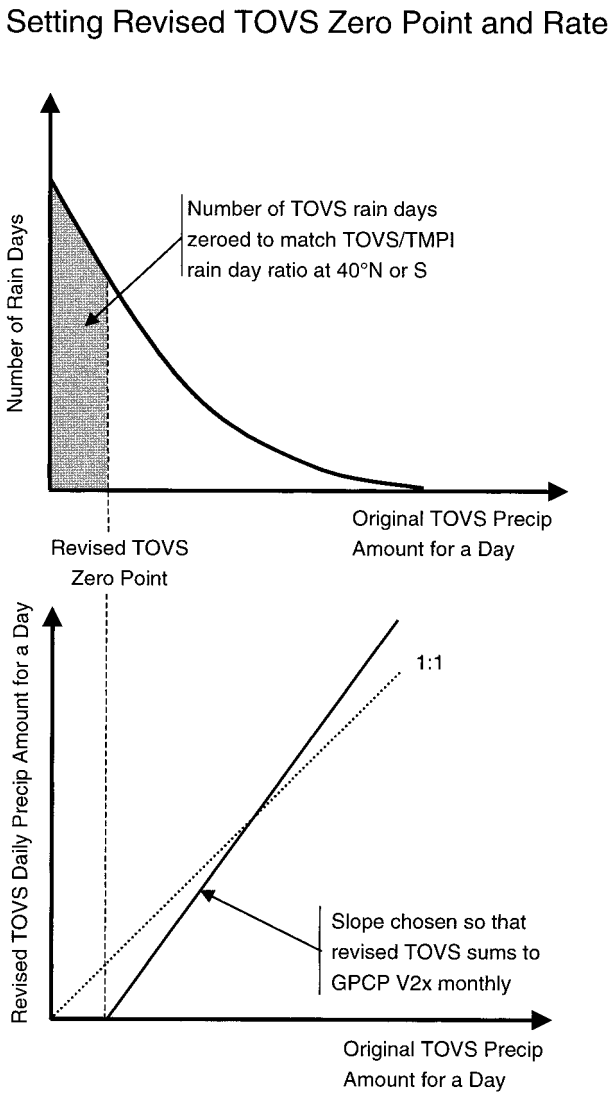

FIG. 6. Schematic diagram of the procedure for revising TOVS. In each grid box a revised zero point is established (top) and applied to transform precipitation rate (bottom).

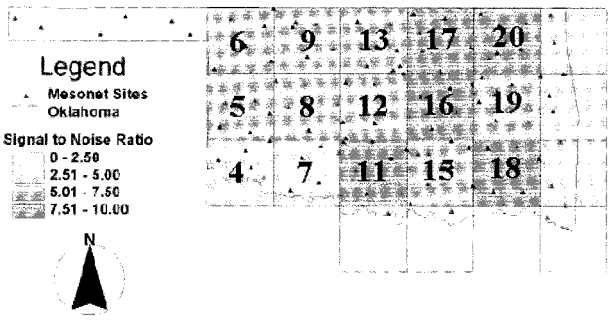

FIG. 7. Locator map of Oklahoma Mesonet stations (dots), 1° × 1° lat/long grid boxes used in this study (numbered boxes), and signal-to-noise ratio computed for the Mesonet analyses used in this study (shading).

becomes serious for this particular month. We also note that monthly sums of GPROF have significant differences from monthly sums of the TMPI (i.e., the SG field, not shown), demonstrating that the GPROF fractional occurrence can be used to formulate the TMPI without GPROF precipitation rates somehow affecting the computation.

3. Rescaled daily TOVS

Outside the latitude band covered by the merged IR dataset (40°N–40°S) it is necessary to base the 1DD on a different dataset. We selected the precipitation estimates that are computed as part of the Susskind et al. (1997) Television and Infrared Observation Satellite (TIROS) Operational Vertical Sounder (TOVS) Pathfinder Path A dataset. The TOVS Path A algorithm uses an atmospheric model to generate a first guess for retrieval of various atmospheric parameters, including cloud-top pressure, fractional cloud cover, and relative humidity profile from NOAA-series satellite data. The precipitation algorithm is a regression between these parameters and surface data stratified by latitude, month, and land/ocean surface type. The result is instantaneous pixel-by-pixel precipitation estimates. TOVS precipitation was chosen for the 1DD based on global coverage, reasonable performance, and the authors' previous experience with monthly accumulations of this product in developing the GPCP version 2 SG product. The influence of the model-generated first guess on the final rescaled TOVS precipitation values is currently under study by the authors, but it is believed to be small. The TOVS precipitation estimates are provided as daily averages on a 1° × 1° global grid.

We find that the number of rain days in TOVS is systematically high in comparison with the TMPI for all months and locations. As well, we wish to ensure that the daily values outside 40°N–40°S sum to the monthly GPCP SG. As a first solution to these issues, we reduce the number of TOVS rain days in a month at each grid box as follows: We compute the ratio of the zonal average number of TMPI rain days in the month to the same for TOVS separately for 39°–40°N and 39°–40°S. Then the number of TOVS rain days for the month at each point in an entire hemisphere is scaled by the corresponding ratio (i.e., 39°–40°N for the Northern Hemisphere). We achieve this smaller number of rain days (in the month for the grid box) by zeroing the smallest rain accumulations (Fig. 6). The largest daily rain amount to be zeroed is labeled as the ''revised zero point.'' The remaining rain days are linearly rescaled to sum to the monthly SG.

An additional minor issue in the original TOVS estimates is a scatter of missing grid values at high latitudes due to the forward scheme used to remap data from satellite to geographical coordinates. We choose to smoothly fill these holes from surrounding data because they are an accident of the gridding scheme.

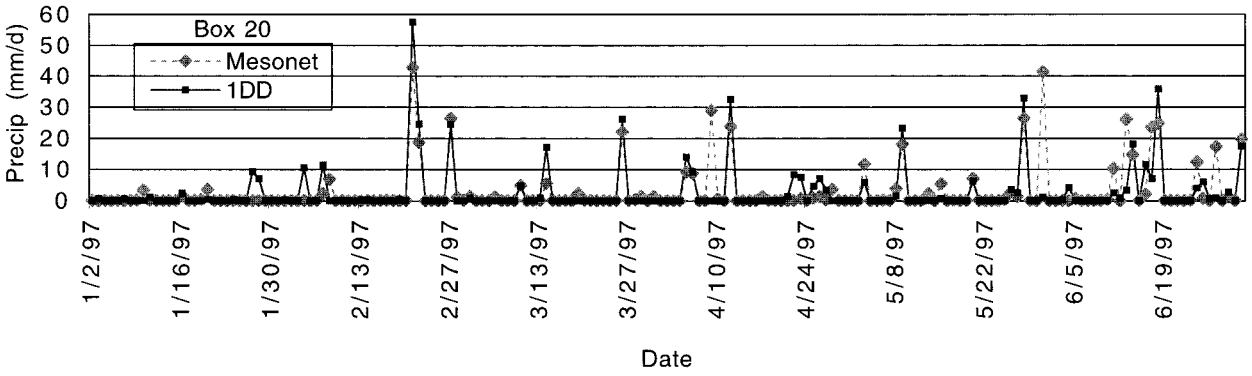

FIG. 8. Plot of the 1DD (solid line, black squares) and Mesonet (dashed line, gray diamonds) daily precipitation in millimeters per day over the first six months of 1997 in box 20.

The resulting revised TOVS estimates show good agreement with the TMPI across the 40°N and 40°S data boundaries. However, enough discrepancy remained on daily maps that smoothing is performed at the boundaries. Specifically, on each day the differences between TMPI and revised TOVS estimates are computed for each of the 39–40°N and 39–40°S grid boxes, then the difference fields are linearly tapered to zero at 50°N and 50°S, respectively, and added to the revised TOVS. Some spurious ''feathering'' occurs near the edge of the TMPI domain, but the general effect is beneficial.

4. Validation

a. Oklahoma Mesonet

An initial validation was carried out over Oklahoma for the period of January 1997–December 1998 for the 1DD using the Oklahoma Mesonet rain gauge data. Mesonet data were used as the validation because the network is fairly dense and none of the stations contributes to the monthly scaling carried out in the 1DD. Figure 7 shows the signal-to-noise ratio (shading) and reference numbers for the $1° \times 1°$ boxes over Oklahoma. A higher signal-to-noise ratio indicates there is less error in the Mesonet estimate associated with that box (Morrissey and Greene 1998). This information was used to delete boxes 4 and 7 as having insufficiently robust estimates for gridbox values. For brevity, single-box results are displayed for box 20, except as noted.

A plot of the 1DD (solid line, black squares) and Mesonet (dashed line, gray diamonds) daily precipitation over the first six months of 1997 (Fig. 8) is representative of the time series plots over the entire 2-yr period of record. The two time series are clearly related, with dry and wet periods showing agreement. Over the entire 1997–98 record the correlation coefficient for box 20 is

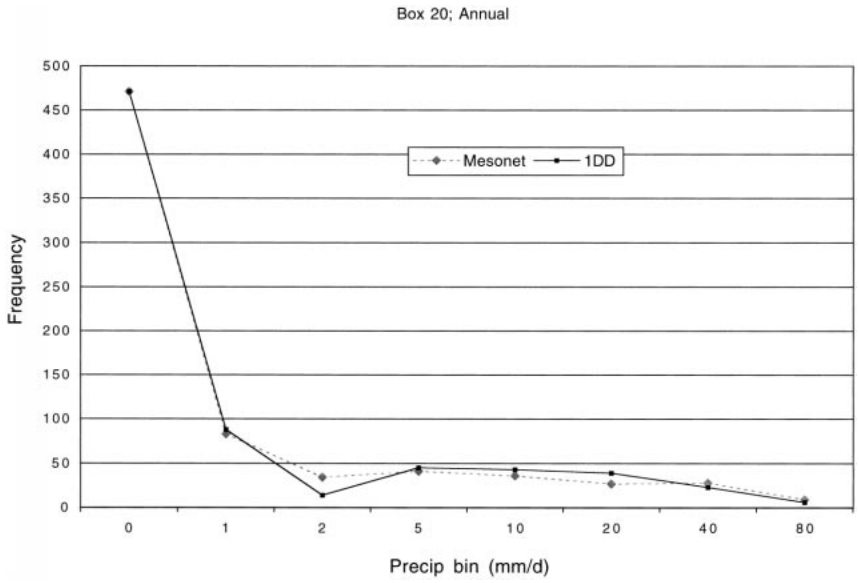

FIG. 9. Histograms of daily precipitation amounts for the 1DD and Mesonet (both as in Fig. 11) accumulated for 1997–98 in box 20.

0.76. A closer look shows that the histograms of daily precipitation amounts for the 1DD and Mesonet accumulated from the 2 yr of data are very similar (Fig. 9). The 1DD has the same number of rain days as the Mesonet, although it bunches slightly more cases in the intermediate range of precipitation rates (5–20 mm day^{-1}). At the seasonal timescale the results (not shown) are similar to Fig. 9, with autumn [September–October–November (SON)], winter [December–January–February (DJF)], and spring [March–April–May (MAM)] showing excellent agreement between 1DD and Mesonet, while summer [June–July–August (JJA)] drives the differences in the annual histograms.

The bias (defined as the 1DD mean divided by the Mesonet mean) and mean absolute error of the daily values were produced for overlapping 3-month periods for each box. The zero–zero points were not removed from the bias calculation, but they *were* removed from the calculation of the mean absolute error. The bias in box 20 (Fig. 10, top) reveals a semiannual fluctuation, with underestimation during the spring and autumn, nearly unbiased values during the summer, and overestimates in winter. The annual-average bias is 0.97. Since the 1DD is scaled to the monthly SG, and since SG values are dominated by the gauge analysis in most land areas, it appears that there are systematic seasonal differences between the Mesonet and Global Precipitation Climatology Centre gauge analyses.

The mean absolute error (Fig. 10, middle) peaks during the early autumn and displays a minimum during the winter. Such variation could result from changes in the character of the precipitation. Specifically, for a fixed set of gauge sites, stratiform precipitation characteristic of the cool season typically yields more accurate area averages, while the warm season's convective precipitation is harder to correctly observe because convection usually has smaller spatial scales. Nonprecipitating cirrus is a year-round problem for the IR-based TMPI; in the cool (stratiform) season the principal problem is frontal bands, while in the warm (convective) season it is transient convective anvils. Variations in error could also result from changes in the mean precipitation because precipitation errors tend to scale with mean precipitation amount (Huffman 1997). In the present case summer convection and maximum average observed (Mesonet) precipitation (Fig. 10, bottom) reinforce each other, leading to the annual cycle in mean absolute error. Future work will focus on the relative importance of changes in precipitation type and mean precipitation rate.

The scatterplots of daily values in box 20 for the summer and winter seasons (Fig. 11) reveal a higher correlation during winter than during summer, which is consistent with the absolute error results. The scatterplots also show fewer outliers during winter than during summer. Each scatterplot includes the best-fit line (heavy solid), the associated linear equation, and the R^2 value. Note that the days for which both the Mesonet and 1DD estimates equaled zero were not removed from the scatterplots, which results in a cluster of points at the origin and tends to tie the best-fit line to the origin. The light dotted line is the one-to-one line. The best fit shows the 1DD overestimating large precipitation values in winter, while there is a large, nearly unbiased scatter in summer. The intercept of the best-fit line is close to zero in both seasons, and positive.

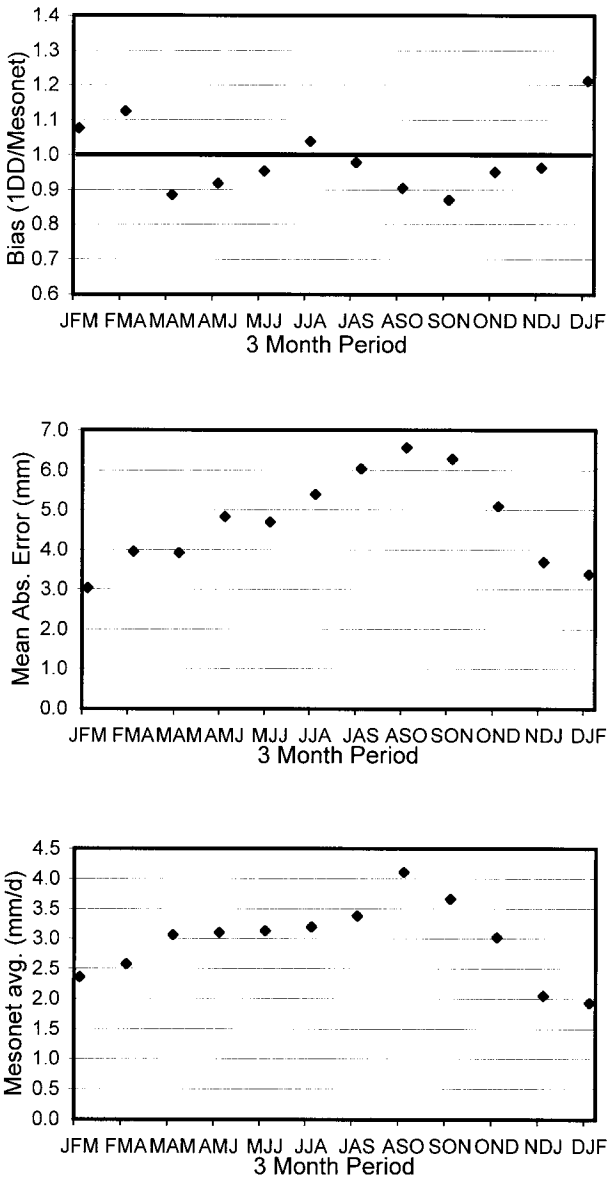

FIG. 10. Bias, computed as the ratio of average daily 1DD to average daily Mesonet (top); mean absolute error of daily 1DD from daily Mesonet (mm day^{-1}) (middle); and average daily Mesonet (mm day^{-1}) (bottom). All quantities are computed for box 20 as 3-month ''climatologies'' for the period 1997–98.

Looking more broadly, we computed the average of the 13-box correlation coefficients for daily values in each season, as well as the entire record, and compared them with the seasonal and annual correlation coeffi-

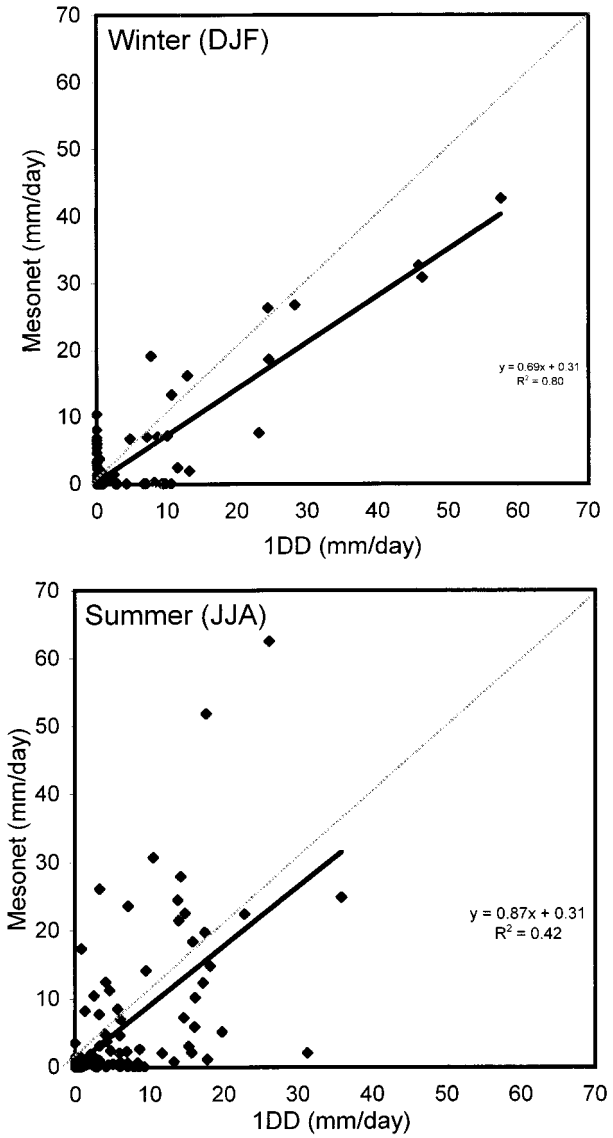

FIG. 11. Scattergrams of daily Mesonet data vs daily 1DD (mm day^{-1}) for box 20 for the Dec–Feb winter (top) and Jun–Aug summer (bottom) seasons. The thin dashed line is the 1:1 line; the heavy solid line is the best-fit line, whose equation and R^2 are also shown.

cients of the 13-box average daily rainfall values (Table 1). As expected, the area averaging improves the correlations significantly, in the range of 15%. Summer shows the greatest improvement, implying that box-to-box fluctuations are largest in that season, consistent with a higher incidence of convective activity.

b. Additional information on 1DD quality

Validation of a global product tends to be difficult because validation sites similar to the Oklahoma Mesonet are not available across the full range of climatic conditions. However, several studies have already been carried out with the beta-test version of the 1DD, which is very similar to the operational version.

TABLE 1. Average over 13 1° × 1° latitude boxes covering most of Oklahoma (all numbered boxes, except 4 and 7 in Fig. 10) of correlation coefficient between daily Mesonet precipitation analyses and daily 1DD precipitation estimates for the seasons and the total dataset, the root-mean-square difference (rms) among the 13 correlation coefficients in each average, and the seasonal and annual correlation coefficients for daily values averaged over the same 13 boxes.

Season	Box-by-box correlation coefficient averaged over 13 boxes	Rms of box-by-box correlation coefficient averaged over 13 boxes	Correlation coefficient of 13-box daily average
Winter	0.668	0.168	0.791
Spring	0.773	0.071	0.884
Summer	0.618	0.135	0.798
Autumn	0.699	0.141	0.781
Annual	0.700	0.101	0.816

A first comparison against the Baltic Experiment precipitation data (Rubel and Rudolf 1999) demonstrates reasonable performance across both warm and cold seasons for area averages over the entire Baltic Sea drainage basin. They find that the monthly averages are nearly unbiased and that the day-to-day occurrence of area-average precipitation is well-represented. The former indicates that the GPCP SG is relatively accurate in this region, while the latter shows that the rescaled TOVS, which provides the estimates over the entire Baltic, is capturing the occurrence of precipitation events on the regional spatial scale.

E. Ebert (2000, unpublished manuscript) validated the 1DD against a 6000-gauge dataset over Australia, which is entirely covered by TMPI estimates. She found that the 1DD performed well in tropical wet season conditions, while it had trouble detecting light rain in dry tropical conditions and in general in midlatitude winter conditions. She attributes many of the errors to the known deficiency in discriminating nonprecipitating cirrus clouds by simple IR thresholding procedures.

Modeling studies of discharge by a number of rivers around the globe (Nijssen et al. 2001) indicate that the 1DD appears to be systematically low in regions of complex terrain, such as the Columbia River, while providing apparently unbiased results in regions of gentler topographic relief, such as the Mississippi River. Nijssen et al. suggest that the gauge analysis, which dominates the GPCP SG (and therefore the 1DD bias) over land, might systematically underestimate precipitation in complex terrain because terrain height effects are not considered.

More generally, the GPCP SG has proved competitive with other monthly rainfall products, for example those being produced in the Tropical Rainfall Measuring Mission (TRMM; Kummerow et al. 2000). Accordingly, we believe that accumulations of the 1DD should be approximately unbiased in regions that do not suffer from the problems noted above. Along the same lines, qual-

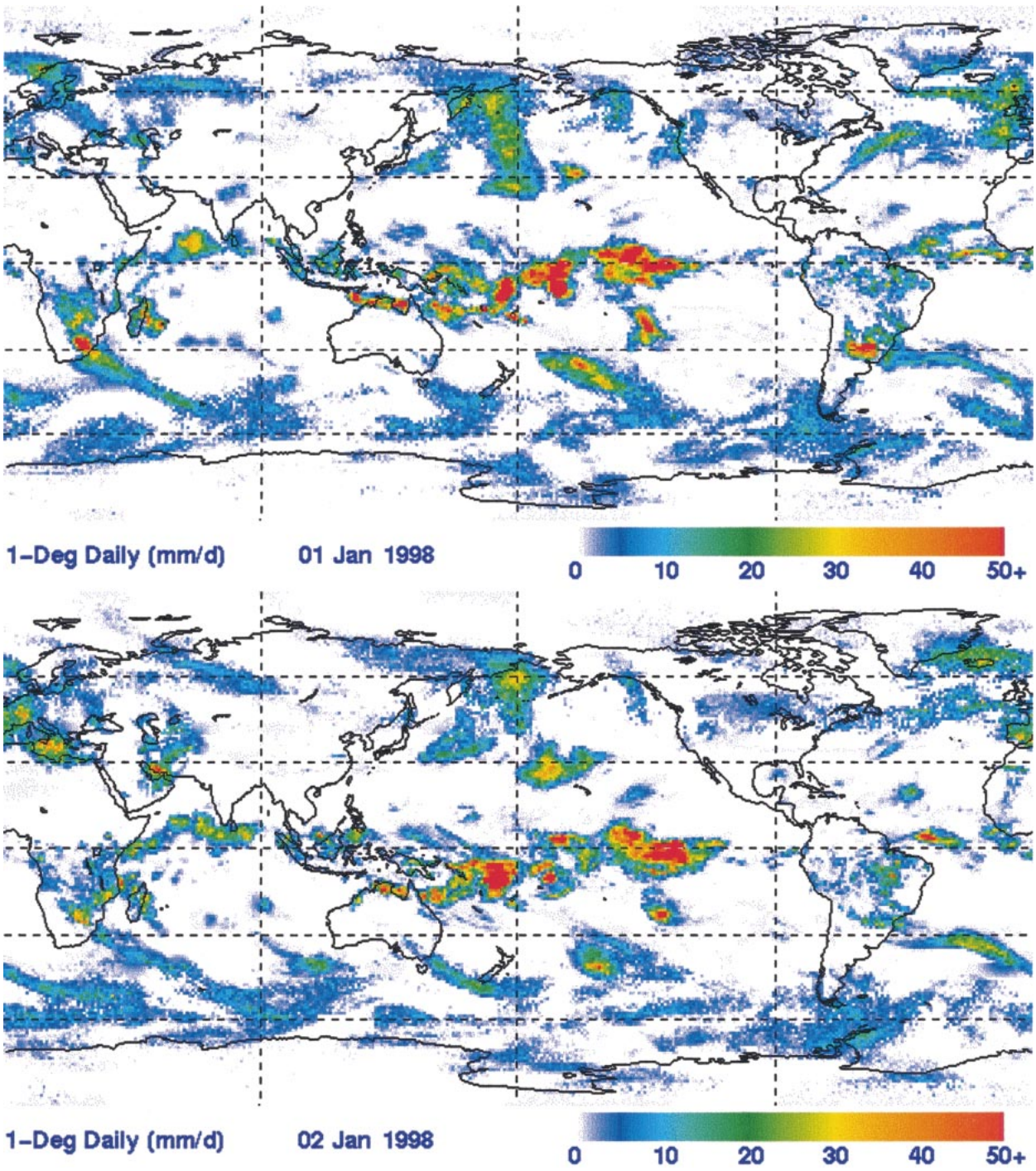

FIG. 12. 1DD images for (top) 1 and (bottom) 2 Jan 1998 in millimeters per day.

itative comparisons among the GPROF 6.0 results for SSM/I, the TRMM Microwave Imager results, and TRMM precipitation radar results indicate that SSM/I-GPROF occurrence of rain is reasonably close to that in the other two datasets for the cases of substantial rain areas that we have examined.

5. Examples

The 1DD has been computed for 1 January 1997–31 December 1999, and new months continue to be appended a few months after real time. The days 1–2 January 1998 (Fig. 12) are typical of the estimates. Ac-

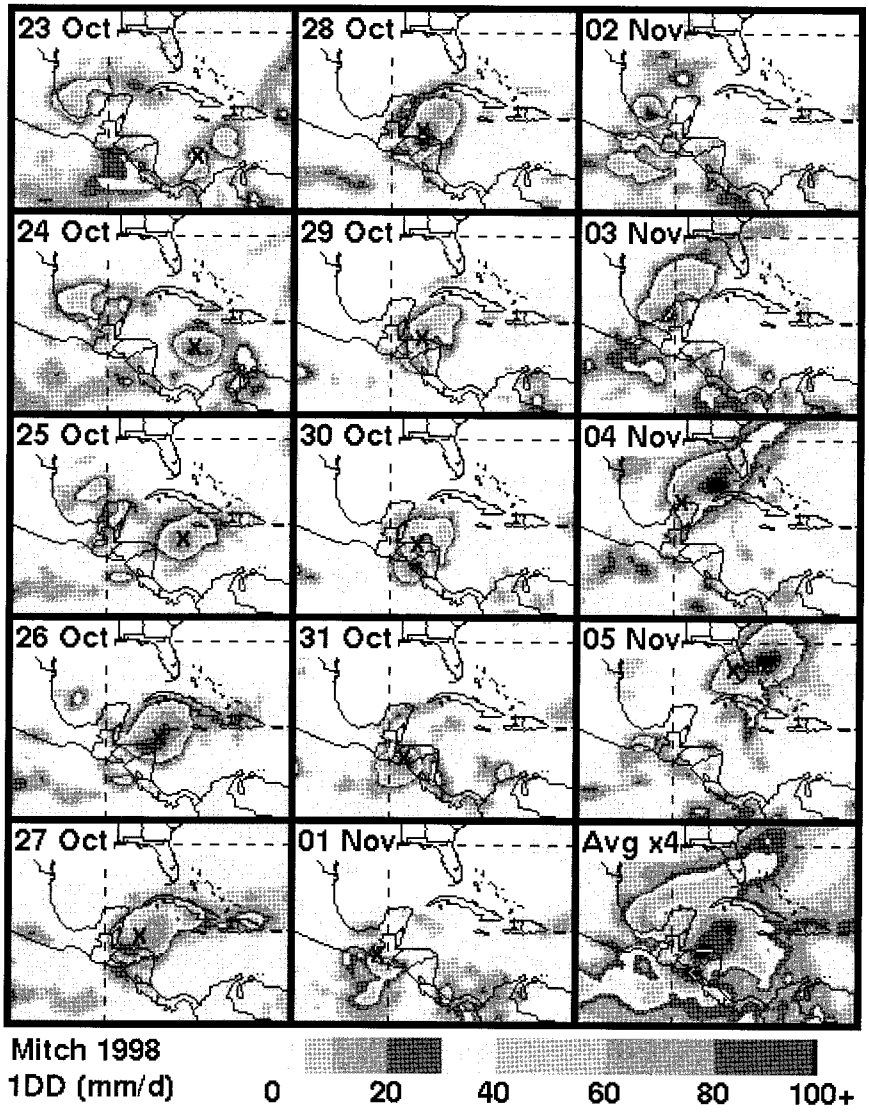

FIG. 13. Bilinearly interpolated 1DD images in millimeters per day for 23 Oct–Nov 1998, illustrating the precipitation associated with Hurricane Mitch. The black Xs denote Mitch's 1200 UTC position on each day for which it was available (storm identity was lost during much of 2–3 Nov as it traversed southern Mexico into the Bay of Campeche). The lower-right-hand panel displays the 14-day average, multiplied by 4 to fit the same gray-shade key.

tivity in the tropical Pacific reflects the significant El Niño in progress at the time. The day-to-day traceability of the storm system across the North Pacific is typical of 1DD's performance. Continuity across the January–February 1998 month boundary was analyzed by applying the ''wrong'' month's coefficients (i.e., January's in February and vice versa) to generate 1DD estimates for 10 days on either side of the month boundary. The results are quite reasonable; about 40% of the nonzero grid box values generated with wrong coefficients are within ±5% of the ''real'' estimates, and approximately 65% are within ±25%. It is true that the differences have regional coherence, so more-gradual transitions between sets of coefficients should be considered in a future release of the data.

Focusing on a particular event, Fig. 13 shows the progression of Hurricane Mitch in late 1998. (Note that the color bar scale covers twice the range of that in Fig. 12.) This storm moved northwest in the western Caribbean, then stalled just offshore of northern Honduras. Mitch lost strength as it meandered across western Honduras, but a remnant circulation wandered west-northwest and emerged in the Bay of Campeche. It rejuvenated to tropical storm status, moved quickly northeast across Florida, and became extratropical. This dataset allows the events reported on land to be seen in the

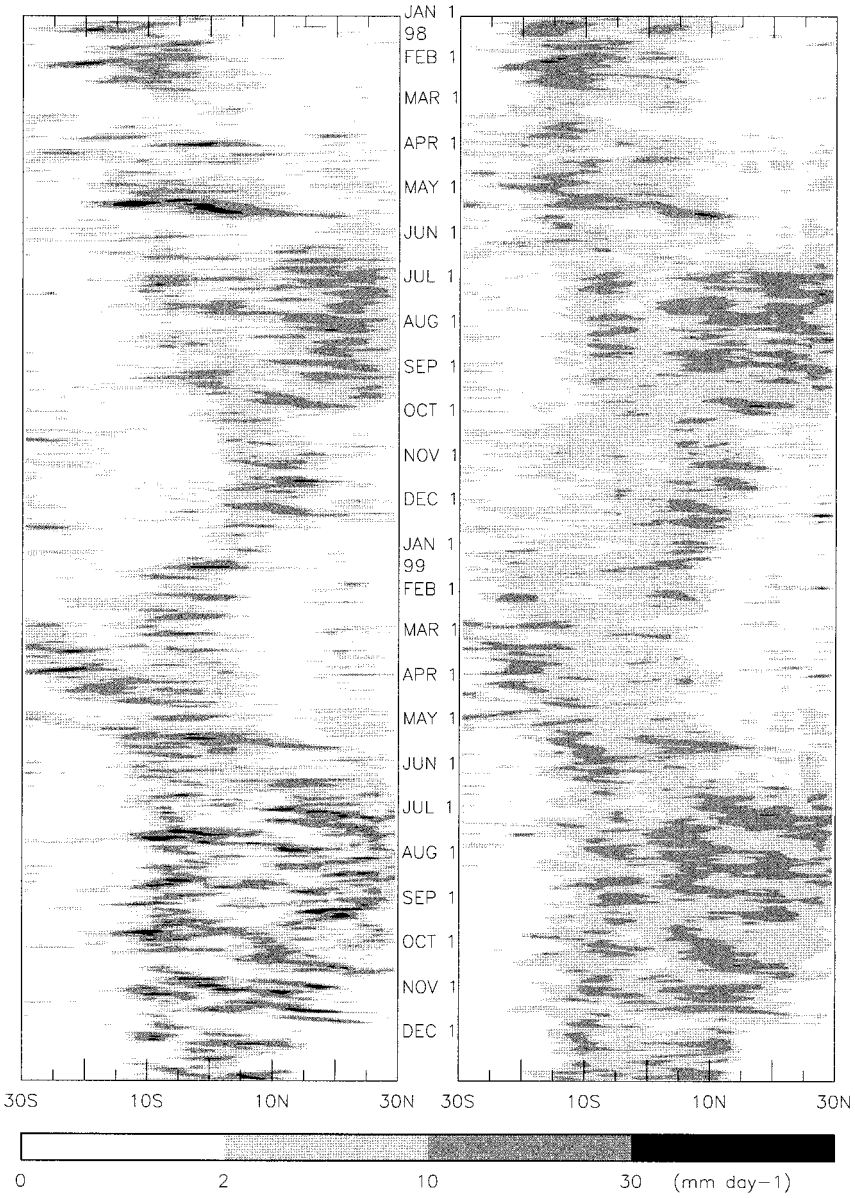

FIG. 14. Time–latitude diagrams (mm day^{-1}) of (left) 1DD and (right) NCEP–NCAR reanalysis daily data for the period of 1 Jan 1997–31 Dec 1998. The diagram extends over 30°S–30°N latitude, and each value is an average over the longitudes 85°–95°E.

context of the storm's complete rain production. Individual daily totals were consistent with values for other tropical storms, but the slow forward speed, looping path, and orographic focussing promoted severe flooding across Honduras and Nicaragua.

The 1DD is particularly useful for forming regional/temporal averages of the user's choosing. For example, the Indian monsoon is summarized in Fig. 14, which displays time–latitude diagrams for 1997–98 of daily precipitation averaged over 85°–95°E (roughly the span of the Bay of Bengal) displayed for the band 30°N–30°S. For 1DD (Fig. 14, left panel), the main envelope of precipitation broadens from the equatorial Indian Ocean (just west of Indonesia) to include the Bay of Bengal in late boreal spring and then retreats six months later, following the annual march of the sun. The figure shows spectacular, short-lived precipitation events due to averaging over a relatively small area. Careful inspection of Fig. 14 shows that the contours tend to be tilted toward the lower right, indicating that many events move south to north, occasionally from well south of the equator (e.g., see May in both 1997 and 1998). For comparison with the observed data (Fig. 14, left panel), similarly processed National Centers for Environmental

Prediction–National Center for Atmospheric Research (NCEP–NCAR) reanalysis estimates (Kalnay et al. 1996) are shown in the right panel of Fig. 14. There is fair agreement, even at the daily scale. The NCEP–NCAR reanalysis tends to have more widespread light precipitation than the 1DD and somewhat lower peak values. As a result, the 1DD distinguishes more clearly between active and break periods in the summer. Such differences are qualitatively consistent with the performance that the authors have seen in the reanalysis, but the quantitative implication depends on further research.

6. Concluding remarks

The One-Degree Daily (1DD) precipitation estimation technique is a complete first-generation procedure for estimating global daily precipitation on a $1° \times 1°$ grid. The algorithm contains two parts; the Threshold-Matched Precipitation Index over the latitude band of 40°N–40°S based on a merged geo-IR dataset with leo-IR fill-in, and a rescaled TOVS at higher latitudes based on the Susskind et al. (1997) TOVS precipitation estimates. Both are designed to sum to the GPCP version 2 monthly satellite–gauge combination. The TMPI reflects the frequency of precipitation occurrence computed from SSM/I, and precipitation occurrence in the rescaled TOVS is adjusted to the TMPI at 40°N and 40°S separately. The 1DD has been computed for 1 January 1997–31 December 1999, and additional months are being computed a few months after real time. The time series of global images show strong continuity from day to day and across the 40°N and 40°S data boundaries. Initial validation studies show that mean absolute errors are relatively large, as one would expect from cloud-based methods at fine time- and space scales. On the other hand, users should see better results if they average the 1DD fields in space or time. The key advantage of the 1DD is its flexibility in allowing users to compute these averages according to their own requirements while maintaining consistency with a standard larger-scale product (the GPCP SG).

The GPCP accepted the 1DD as an official GPCP product in August of 2000. The 1DD is now available from World Data Center A (located at National Climatic Data Center, Asheville, North Carolina).[1]

Further development of the 1DD is expected to take a number of directions. First, following standard GPCP practices, fields of error estimates are being prepared to accompany the fields of precipitation estimates, similar to those already available for the GPCP version 2. Second, we expect to work toward releasing individual 3-hourly estimates, although there will be gaps in individual fields at higher latitudes. The major issue in this effort is the importance of the time lag between precipitation and cloud-based estimators. Third, estimates based on low-orbit microwave data will be combined directly with calibrated IR estimates. This might include Special Sensor Microwave Imager, TRMM Microwave Imager, and Advanced Microwave Sounding Radiometer data. Fourth, other sensor systems will be examined for inclusion, including daily gauge data. The last suffers significant difficulties in coverage and time-of-report diversity. Last, we expect to evaluate more-sophisticated IR and TOVS algorithms for possible improvements in accuracy.

Acknowledgments. This research was funded through the TRMM Science Team under the NASA Headquarters TRMM Program Scientist Dr. Ramesh Kakar. The four anonymous reviewers are thanked for thoughtful reviews.

[1] The data can be obtained at http://www.ncdc.noaa.gov/wdcamet.html#GPCP or by contacting Mr. David Smith, NCDC, Room 120, 151 Patton Ave., Asheville, NC 28801-4328. The data are also available from the authors at http://rsd.gsfc.nasa.gov/912/gpcp.

REFERENCES

Adler, R. F., G. J. Huffman, and P. R. Keehn, 1994: Global rain estimates from microwave-adjusted geosynchronous IR data. *Remote Sens. Rev.*, **11,** 125–152.

Arkin, P. A., and B. N. Meisner, 1987: The relationship between large-scale convective rainfall and cold cloud over the Western Hemisphere during 1982–84. *Mon. Wea. Rev.*, **115,** 51–74.

Blackmon, M. L., Y. H. Lee, J. M. Wallace, and H. H. Hsu, 1984: Time variation of 500 mb height fluctuations with long, intermediate and short time scales as deduced from lag-correlation statistics. *J. Atmos. Sci.*, **41,** 981–991.

Crum, T. D., R. E. Saffle, and J. W. Wilson, 1998: An update on the NEXRAD Program and future WSR-88D support to operations. *Wea. Forecasting*, **13,** 253–262.

Huffman, G. J., 1997: Estimates of root-mean-square random error for finite samples of estimated precipitation. *J. Appl. Meteor.*, **36,** 1191–1201.

——, and Coauthors, 1997: The Global Precipitation Climatology Project (GPCP) Combined Precipitation Dataset. *Bull. Amer. Meteor. Soc.*, **78,** 5–20.

Joyce, R. J., and P. A. Arkin, 1997: Improved estimates of tropical and subtropical precipitation using the GOES precipitation index. *J. Atmos. Oceanic Technol.*, **14,** 997–1011.

——, J. E. Janowiak, and G. J. Huffman, 2001: Latitudinally and seasonally dependent zenith-angle corrections for geostationary satellite IR brightness temperatures. *J. Appl. Meteor.*, in press.

Kalnay, E., and Coauthors, 1996: The NCEP/NCAR 40-Year Reanalysis Project. *Bull. Amer. Meteor. Soc.*, **77,** 437–471.

Kummerow, C., and L. Giglio, 1995: A method for combining passive microwave and infrared rainfall observations. *J. Atmos. Oceanic Technol.*, **12,** 33–45.

——, W. S. Olsen, and L. Giglio, 1996: A simplified scheme for obtaining precipitation and vertical hydrometeor profiles from passive microwave sensors. *IEEE Trans. Geosci. Remote Sens.*, **34,** 1213–1232.

——, and Coauthors, 2000: The status of the Tropical Rainfall Measuring Mission (TRMM) after two years in orbit. *J. Appl. Meteor.*, **39,** 1965–1982.

Morrissey, M. L., and J. S. Green, 1998: Using the Oklahoma Mesonet to develop and test a practical sampling error statistic for meteorological time series. *J. Geophys. Res.*, **103,** 8979–8984.

Nijssen, B., G. O'Donnell, D. P. Lettenmaier, D. Lohmann, and E. F. Wood, 2001: Predicting the discharge of global rivers. *J. Climate*, in press.

Rubel, F., and B. Rudolf, 1999: Verification of GPCPs satellite-based

daily precipitation analyses using corrected rain gauge data of BALTEX for the Baltic Sea catchment area. Working Group Biometeor., Institute of Medical Physics and Biostatistics, Veterinärmedizinische Universität Wien, Vienna, Austria. [Available online at http://www-med-physik.vu-wien.ac.at/staff/rub/pro/GPCC/applications.htm]

Susskind, J., P. Piraino, L. Rokke, L. Iredell, and A. Mehta, 1997: Characteristics of the TOVS Pathfinder Path A dataset. *Bull. Amer. Meteor. Soc.*, **78,** 1449–1472.

WCRP, 1986: Report of the workshop on global large scale precipitation data sets for the World Climate Research Programme. WMO Rep. 94, 45 pp. [Available from World Meteorological Organization, P.O. Box 2300, CH-1211 Geneva 2, Switzerland.]

Xu, L., X. Gao, S. Sorooshian, and P. A. Arkin, 1999: A microwave infrared threshold technique to improve the GOES Precipitation Index. *J. Appl. Meteor.*, **38,** 569–579.